PNAS
www.pnas.org

Supplementary Information for

GABA-mediated tonic inhibition differentially modulates gain in functional subtypes of cortical interneurons

Alexander Bryson, Robert John Hatch, Bas-Jan Zandt, Christian Rossert, Samuel Berkovic, Christopher A Reid, David B Grayden, Sean Hill, Steven Petrou**

**Alexander Bryson, Steven Petrou*
Email: *alexander.bryson@florey.edu.au, steve.petrou@florey.edu.au*

This PDF file includes:

Figures S1 to S10
Methods
Table S1 & S2
SI references

www.pnas.org/cgi/doi/10.1073/pnas.1906369117

SI Figures

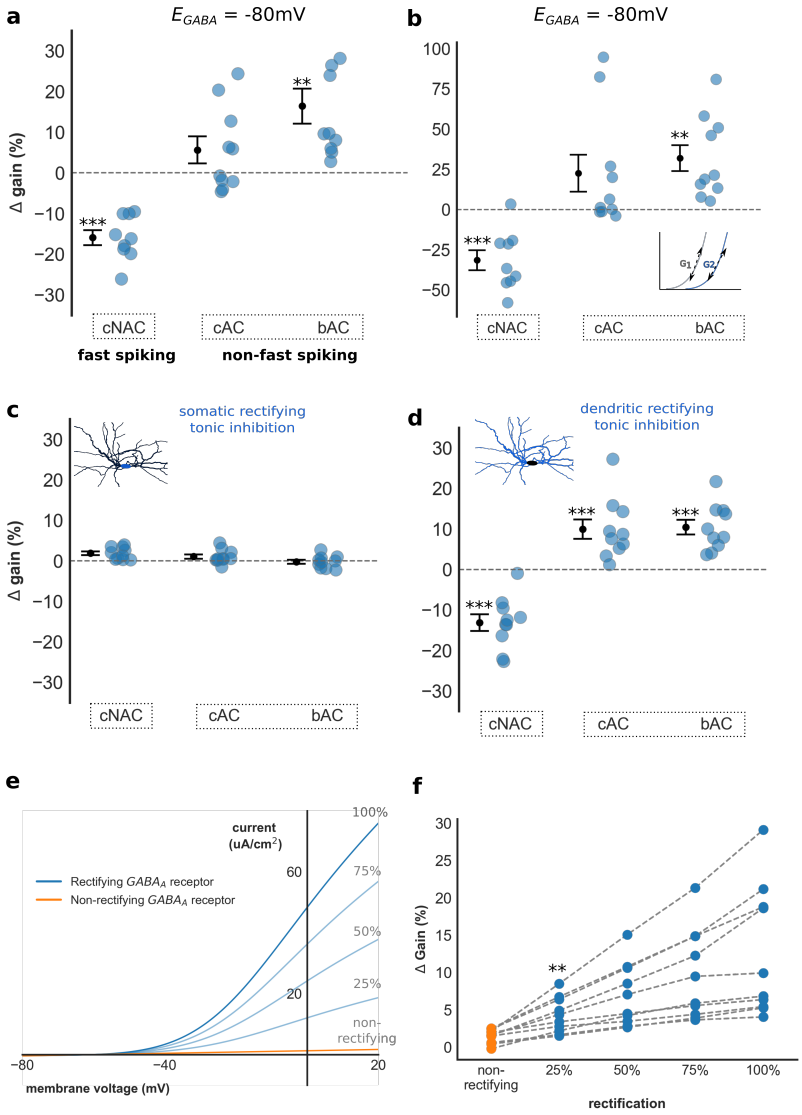

Fig. S1.
a-b) Δ gain in all models grouped by E-type for E_{GABA} = -80mV. Rectifying tonic inhibition produced a significant difference in Δ gain between fast spiking and non-fast spiking E-types (-16.0% ± 1.8 vs 11.0% ± 2.9, Welch's *t*-test, $t(28) = -6.0$, $P < 0.001$). Differential gain modulation was still observed if Δ gain calculated using the gradient of the I-F curve (**b**, -31.5% ± 6.2 vs 27.2% ± 6.9, Welch's *t*-test, $t(28) = -5.3$, $P < 0.001$). If the spatial distribution of rectifying tonic inhibition is restricted to the soma significant changes of Δ gain did not occur (**c**). In contrast, dendritic tonic inhibition produced large differences of Δ gain between E-types (**d**, -13.1% ± 2.0 vs 10.2% ± 1.5, Welch's *t*-test, $t(28) = -9.32$, $P < 0.001$). **e-f)** To investigate the relationship between outward rectification and gain modulation, the magnitude of rectification was varied and Δ gain recalculated for all bAC models (at 25% rectification, tonic inhibition passes 25% of the hyperpolarising current passed at 0mV in the rectifying model). A step-wise increase of rectification produced a step-wise increases of gain in all models. 25% rectification produced a significant increase in Δ gain compared to non-rectifying inhibition (Wilcoxon signed-rank test, $Z = 0.0$, $P < 0.01$). Note: asterix in **a-d** denotes a significant Δ gain value compared to Δ gain = 0%, one-sample *t*-test. *$P < 0.05$, **$P < 0.01$, *** $P < 0.001$.

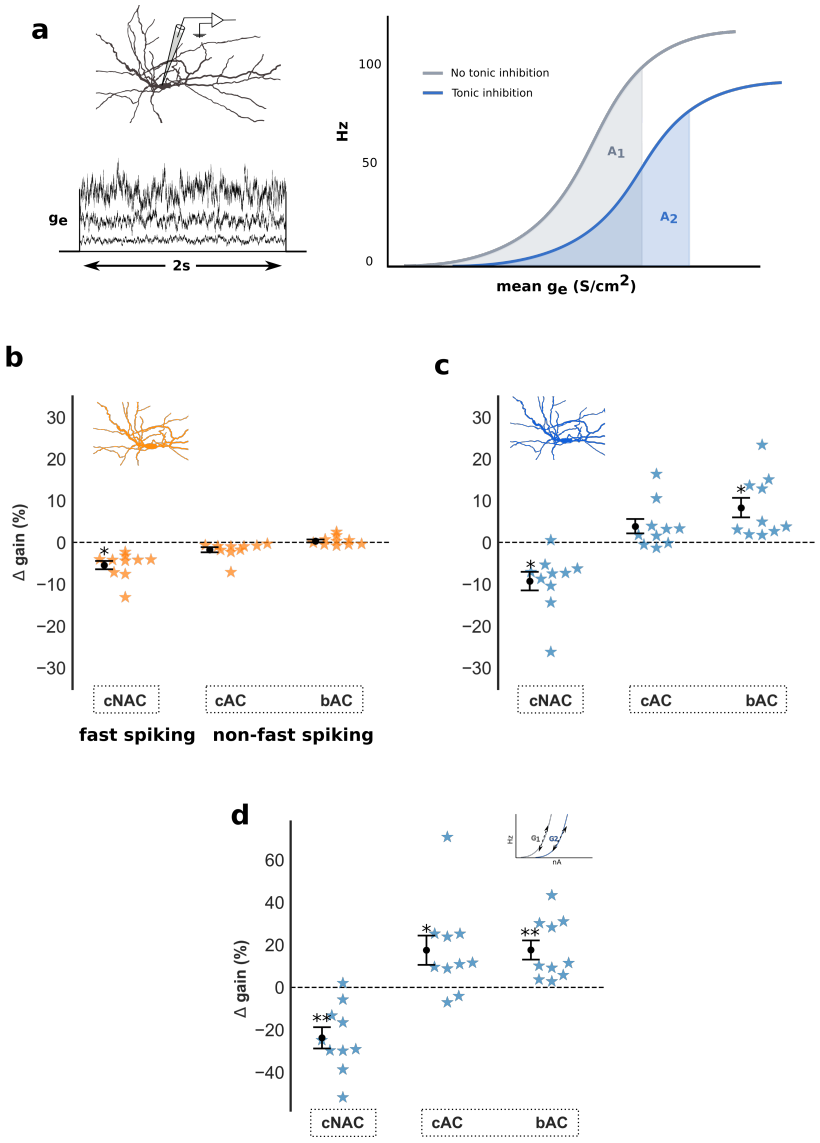

Fig. S2.
a) Excitatory conductance noise (g_e) of increasing mean and variance was injected into the soma and Δ gain calculated using an identical method to **Fig. 1b**. Δ gain in all models grouped by E-type for non-rectifying (**b**) and rectifying (**c**) tonic inhibition. Both rectifying and non-rectifying tonic inhibition induced significant differences in Δ gain between fast spiking and non-fast spiking E-types, however the magnitude of this difference was greater in the presence of rectifying tonic inhibition (-9.3% ± 2.2 vs 6.1% ± 1.5, Welch's *t*-test, $t(28) = -5.7$, $P < 0.001$). Differential gain modulation between fast spiking and non-fast spiking models persisted if gain was measured using gradient of the I-F curve (**d**, -23.7% ± 5.0 vs 17.8% ± 3.2, Welch's *t*-test, $t(28) = 20.0$, $P < 0.001$). Note: Asterix denotes a significant Δ gain value compared to Δ gain = 0%, one-sample *t*-test. $^*P < 0.05$, $^{**}P < 0.01$, $^{***}P < 0.001$.

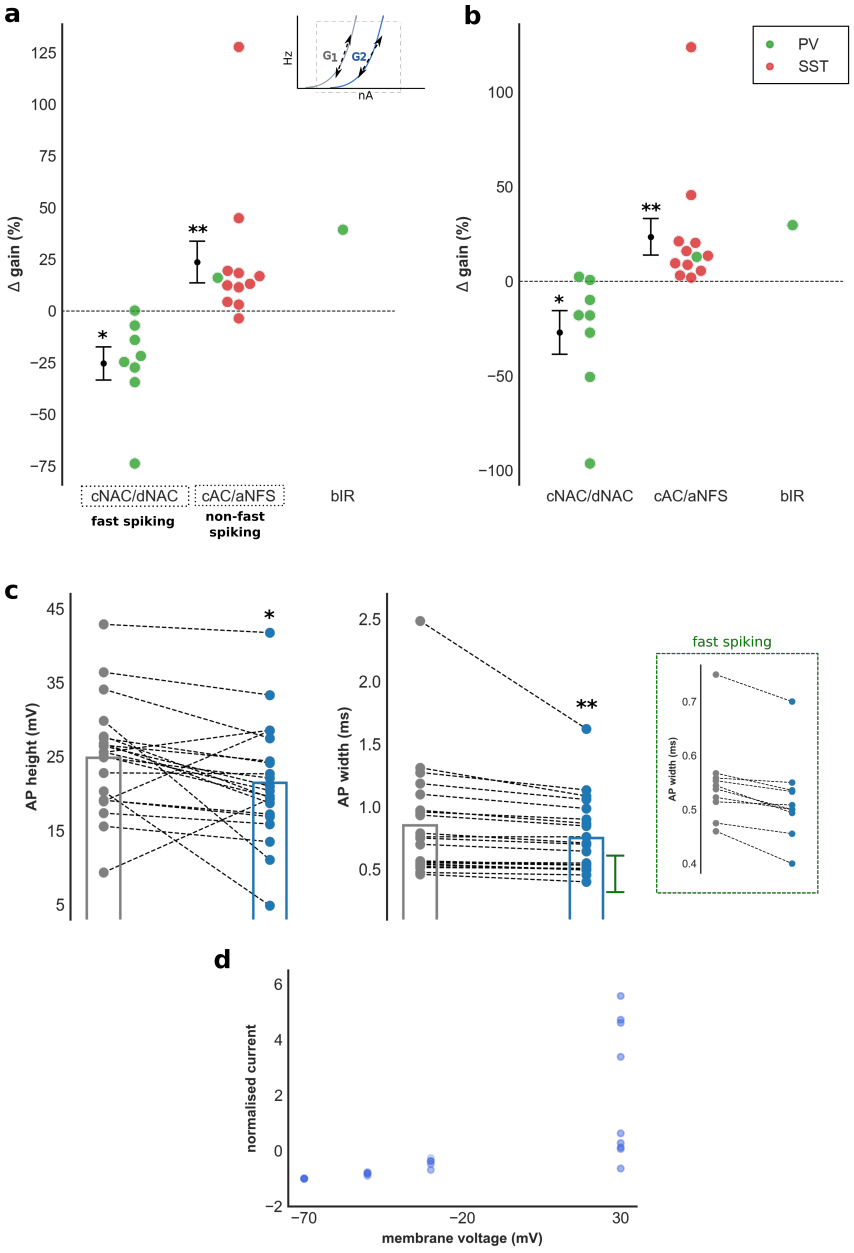

Fig. S3.
Experimental changes in gain (Δ gain) with tonic inhibition. Here, Δ gain is calculated using two additional measures: **a)** change in gradient of the I-F curve at 20Hz, and **b)** change in peak gradient of the I-F curve (see Methods). For both measures, tonic inhibition produced a significant change in Δ gain between fast spiking and non-fast spiking interneurons (two-sided Mann-Whitney U test, $U = 1$, $P < 0.001$ for both **a** & **b**). **c)** Change in AP height and width with tonic inhibition for all experimental recordings. Recordings from fast spiking interneurons shown separately as they have narrower AP width compared to non-fast spiking interneurons. Tonic inhibition reduced AP height ($P < 0.001$) and width ($P < 0.01$), consistent with modelling results (**Fig. 5g**). **d)** I-V relationship of 9 Sst-positive interneurons. Current is normalised to holding current at -70mV. Four interneurons show marked outward current rectification. Note: Asterix in **a** & **b** denotes a significant Δ gain value compared to Δ gain = 0%. *$P < 0.05$, **$P < 0.01$, *** $P < 0.001$.

cAC

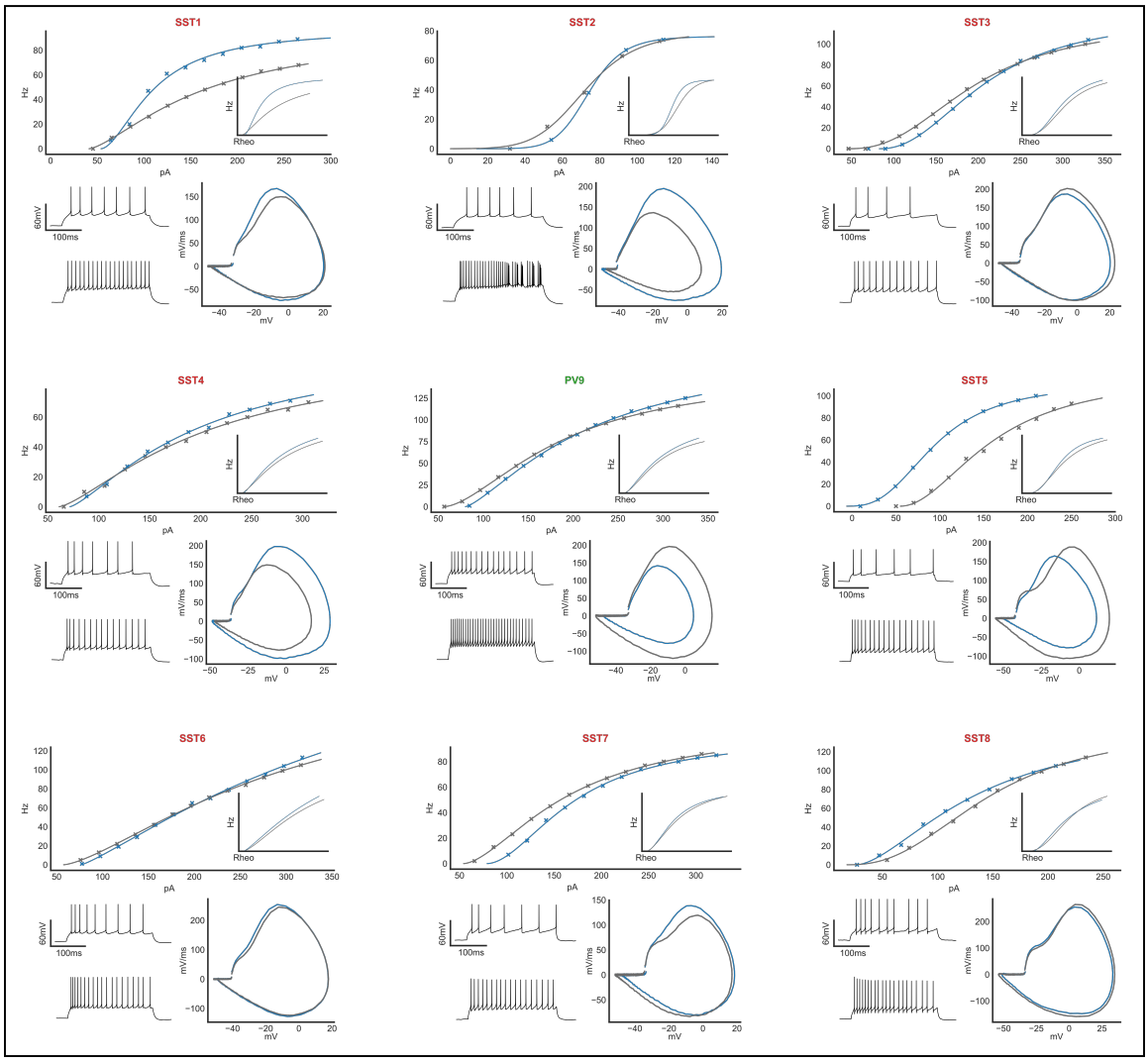
SST1
SST2
SST3
SST4
PV9
SST5
SST6
SST7
SST8
Hz
pA
Rheo
60mV
100ms
mV/ms
mV

cNAC

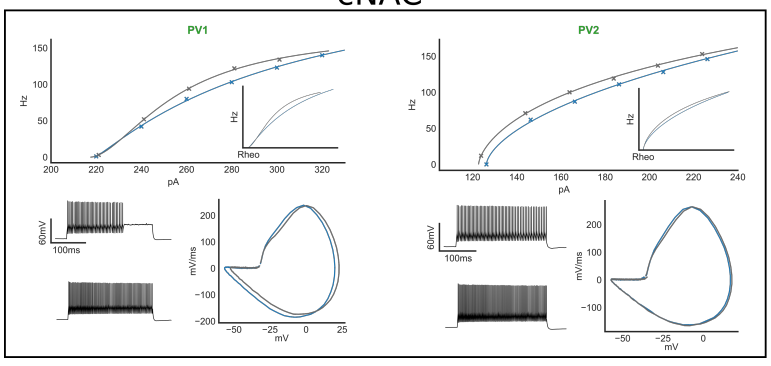
PV1
PV2
Hz
pA
Rheo
60mV
100ms
mV/ms
mV

bIR

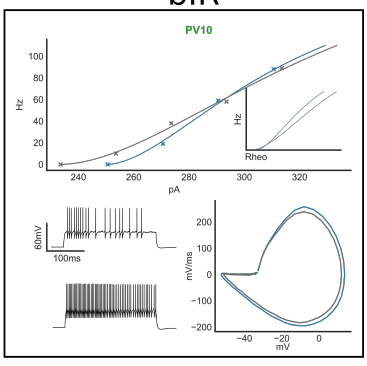
PV10
Hz
pA
Rheo
60mV
100ms
mV/ms
mV

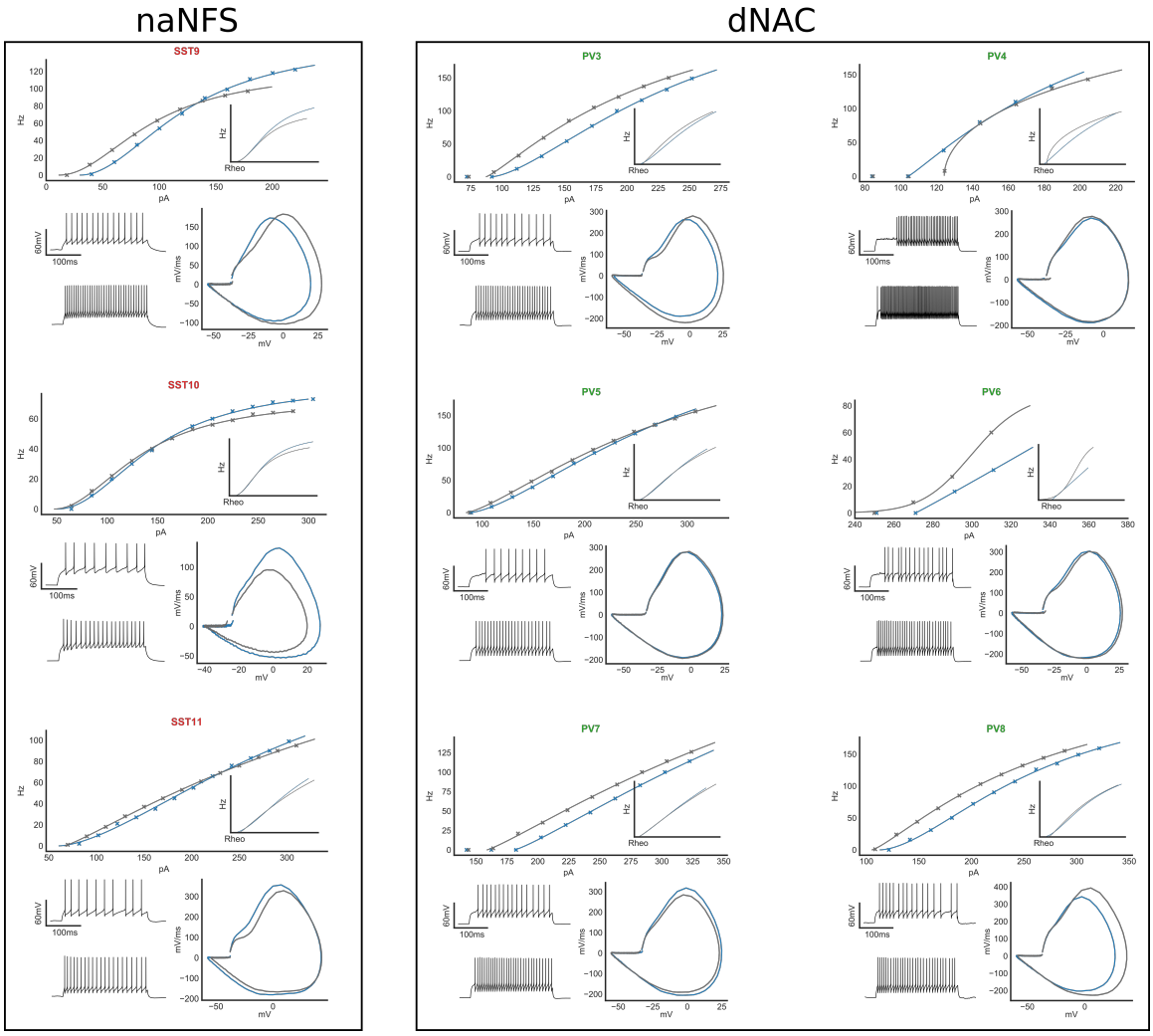

Fig. S4.
I-F relationships of experimental interneuron recordings grouped by E-type. Cell names correspond to **Fig. 3**. Inset shows I-F relationship adjusted for rheobase. Time-voltage traces (lower left) are for rheobase input (top) and 20nA above rheobase (bottom) without tonic inhibition. Lower right shows AP phase portrait at rheobase with (blue) and without (grey) tonic inhibition, adjusted for AP threshold. Phase plot AUC's are summarised in **SI Appendix Fig. S5** and electrophysiologic features for each cell found in **SI Appendix Table S1.**

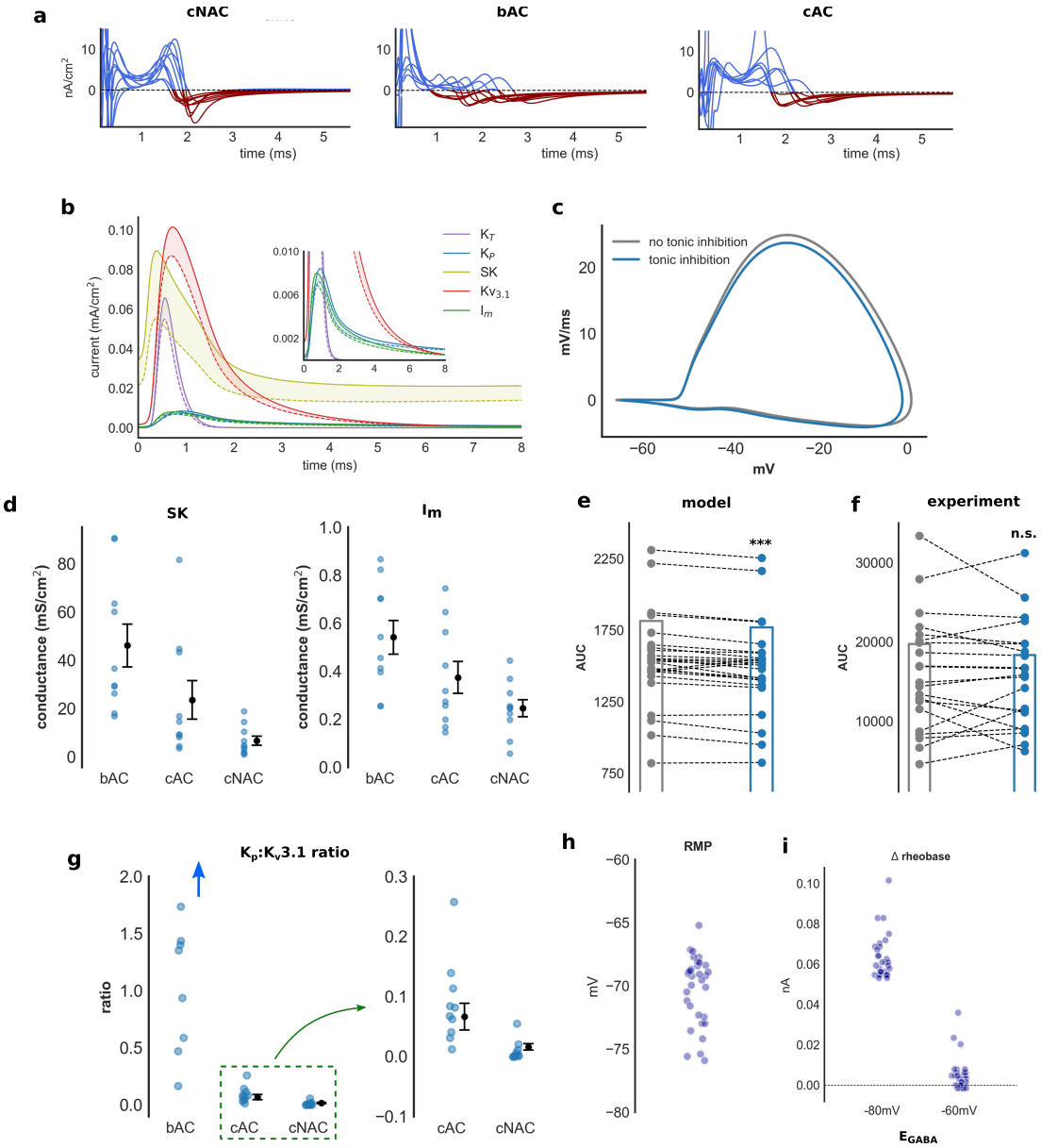

Fig. S5.

a) Δ total membrane current in all models by E-type from AP onset. **b)** Potassium current during an ISI in one model without (solid) and with (dashed) rectifying tonic inhibition from AP onset. Filled region demonstrates change in potassium current, with reduced activation observed in all voltage-dependent potassium channels. **c)** AP phase portrait of one model, and summary of AP phase portrait AUC in all models (**e**) and experiments (**f**) without (grey) and with (blue) tonic inhibition. A significant reduction of AUC was found in models (**c**, Wilcoxon signed-rank test, $P < 0.001$). Although 12/21 recorded interneurons showed reduced AUC this did not reach statistical significance. **d)** Average conductance density (see Methods) of SK and I_m channels that mediate spike-frequency adaptation in models. Non-fast spiking models have higher density of both conductance's (Mann-Whitney U-test, $U = 24.0$, $P < 0.001$ for SK; $U = 41.0$, $P < 0.01$ for I_m). **g)** Ratio of K_P to $Kv_{3.1}$ conductance. Non-fast spiking models had significantly higher ratio's (Mann-Whitney U-test, $U = 4.0$, $P < 0.001$). Two bAC models had ratio's > 6 (blue arrow) and are not shown in this figure (blue arrow). **h-i)** Resting membrane potential (RMP) and change in rheobase for all models with and without tonic inhibition, for two E_{GABA} values. An E_{GABA} of -60 and -80mV is depolarised and hyperpolarised relative to RMP in all models. Channel abbreviations: K_T = transient K; K_P = persistent K; SK = Calcium-activated K.

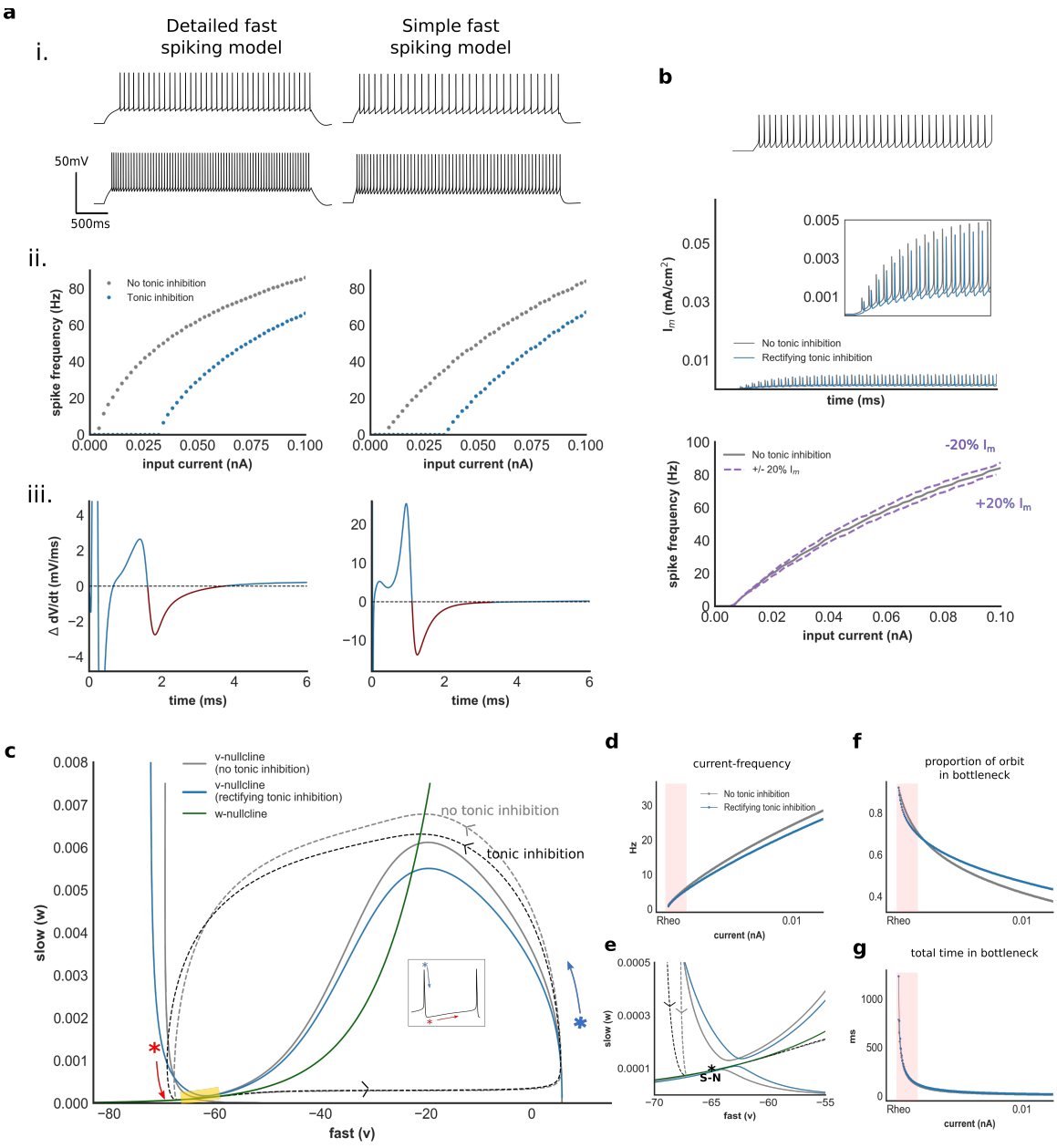

Fig. S6.

a) Electrophysiological features (i), I-F relationship (ii) and change in total membrane current (iii) within a simplified fast spiking models and its detailed counterpart. **b)** I_m current generated by the simple fast spiking model without (grey) and with (blue) tonic inhibition. Impact of changes in I_m current upon gain in the fast spiking model. **c)** Phase-plane of the *v*-*w* subsystem of the fast spiking model, and orbits during AP generation, without and with tonic inhibition. Yellow region denotes bottleneck which occupies 90% of the duration of the orbit at spike onset. **d)** I-F relationship of the *v*-*w* system. **e)** Phase-plane of the *v*-*w* system at the bottleneck. The transition from rest to spiking occurs via saddle-node (S-N) bifurcation. During the AP downstroke and AHP, w deactivates rapidly compared to the fast spiking model, and the trajectory traverses the bottleneck adjacent to the *w* nullcline (c/w **Fig. 6c**). Consequently, reduced activation of *w* with tonic inhibition has minimal impact upon the trajectory through the bottleneck. **f)** Proportion of orbit spent traversing the bottleneck, and proportion of time within the bottleneck (**g**) with increasing input current. Tonic inhibition does not increase the rate of scaling (gain) through this region with increasing input current.

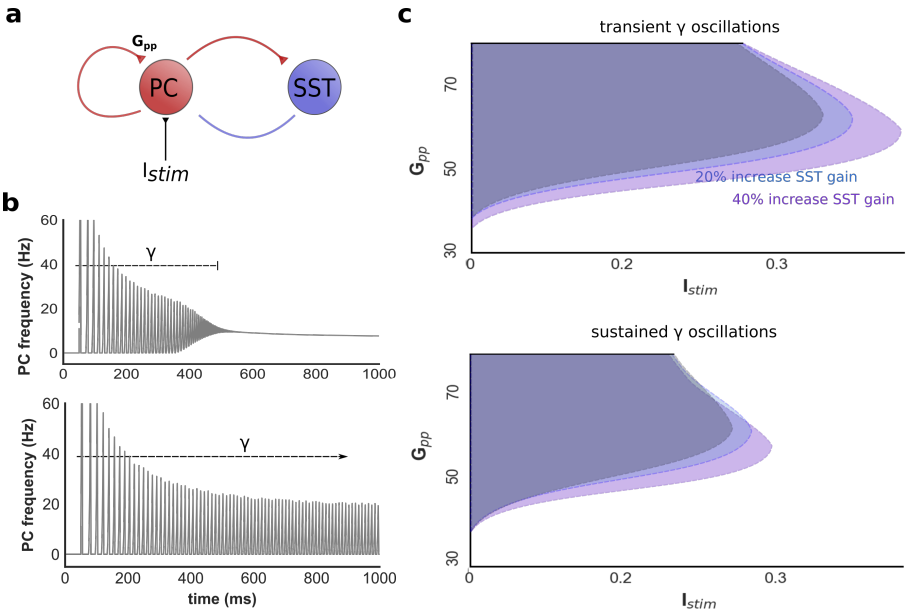

Fig. S7

a) Rate-based network consisting of pyramidal neurons (PC) with recurrent excitatory synapses (synaptic strength = G_{pp}) and reciprocally connected interneurons (SST) providing feedback inhibition. **b)** With sufficient input (I_{stim}) and recurrent excitatory synaptic strength this network generates transient (top) and sustained (bottom) gamma (γ)-frequency oscillations. **c)** Sensitivity analysis demonstrating range of I_{stim} and G_{pp} values over which transient (top) and sustained (bottom) gamma-frequency oscillations occur. Increased SST gain promotes network oscillations over a wider parameter range (grey: baseline, blue: 20% increase, purple: 40% increase).

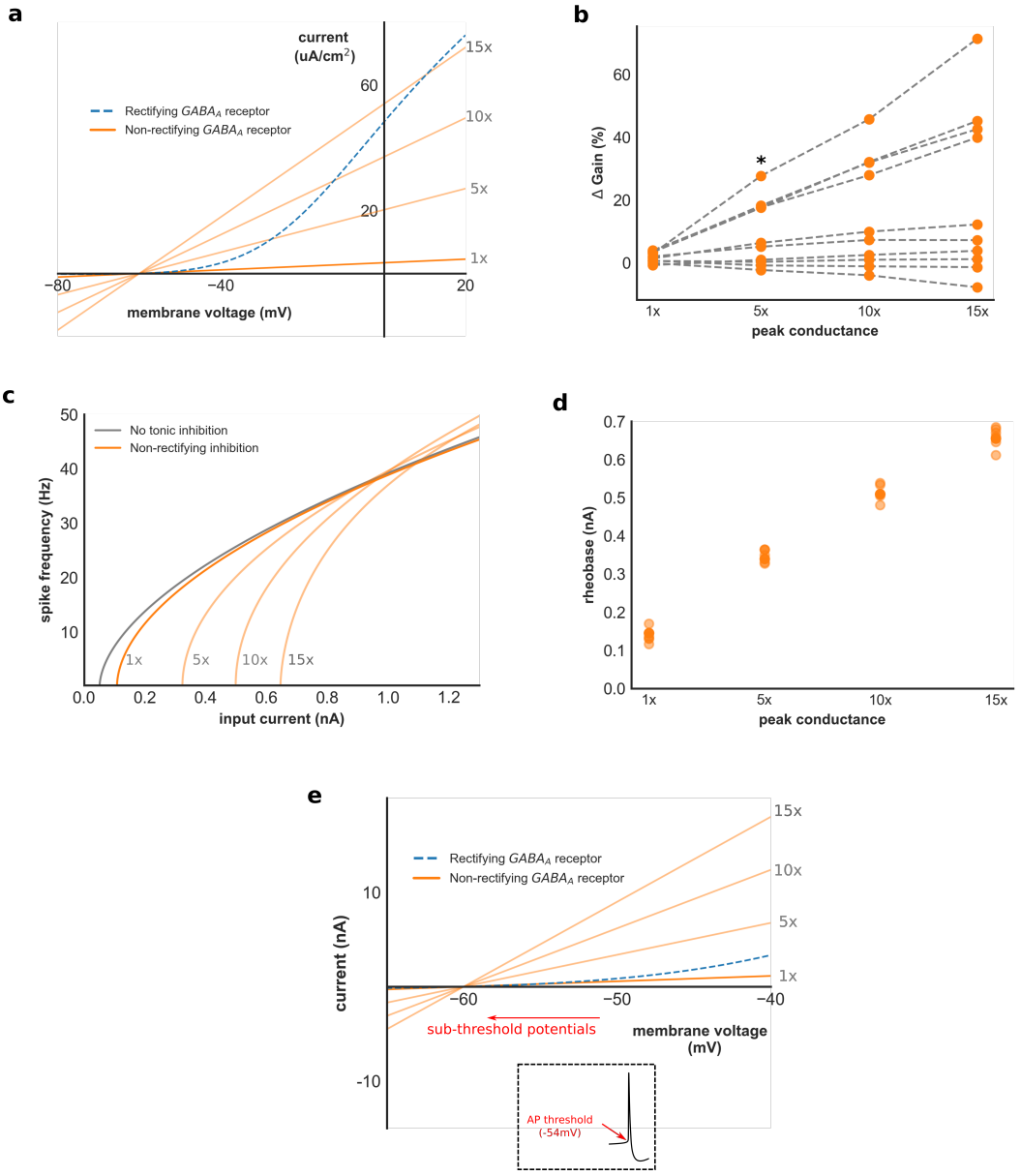

Fig. S8.
Here, we compare the effect of rectifying to non-rectifying inhibition of increasing peak conductance upon neuronal gain. **a)** I-V relationship of rectifying (blue) and non-rectifying (orange) tonic inhibition at 1x, 5x, 10x & 15x the peak conductance used in our models. At 10-15x peak conductance, non-rectifying inhibition generates similar magnitude of hyperpolarising current at depolarised membrane potential to rectifying inhibition. **b)** Δ gain after blockade of non-rectifying tonic inhibition for all optimised bAC models with increasing peak conductance, corresponding to the I-V relationship shown in (**a**). A step-wise increase of Δ gain is observed in 7 models, and large increases in 4 models, with higher peak conductance. A 5x peak conductance value generates a significant increase in Δ gain compared to baseline (Wilcoxon signed-rank test, $Z = 7.0$, $P < 0.05$). **c)** I-F relationship of 1 bAC model for increasing non-rectifying peak conductance corresponding to **a**. Despite increasing gain, large increases of rheobase also occur (all bAC models in **d**). The biophysical basis for increased rheobase is shown in **e**. Compared to rectifying inhibition, non-rectifying inhibition conducts far more hyperpolarising current at subthreshold membrane potential resulting in more input current required to reach AP threshold.

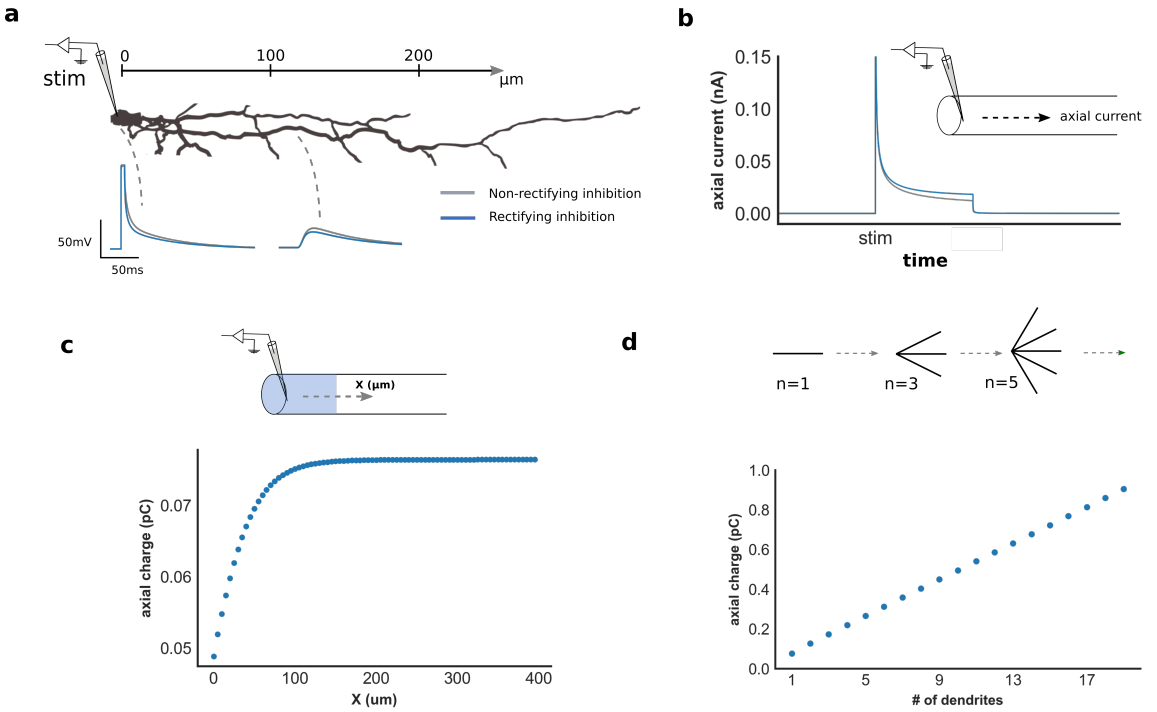

Fig. S9.
Here, the impact of dendritic morphology and spatial distribution of extra-synaptic $GABA_A$ receptors upon enhanced AP repolarisation is explored. **a)** A brief current is injected into a single dendrite eliciting a spike that propagates distally with either rectifying (blue) or non-rectifying (grey) inhibition distributed throughout the dendrite. Similar to our detailed models, the presence of rectifying tonic inhibition attenuates the amplitude of the propagating spike. **b)** Axial current into the adjacent compartment from which the stimulus was applied (positive values denote current flow away from the stimulus). The presence of rectifying tonic inhibition (blue) enhances axial current down the dendrite. **c)** The spatial distribution (X) of tonic inhibition is varied from the site of stimulus while conductance density kept constant. Extending the distribution of rectifying tonic inhibition initially produces a large increase of axial current (here expressed as total charge), but at distances over ~100um exerts minimal further impact suggesting that tonic inhibition has greatest effect upon AP repolarisation at the proximal dendrite. **d)** Additional dendritic branches were added to the compartment in which the stimulus was injected. The presence of additional branches increases the magnitude of axial current, suggesting that more extensive dendritic arborisation will enhance AP repolarisation. pC = picocoulomb.

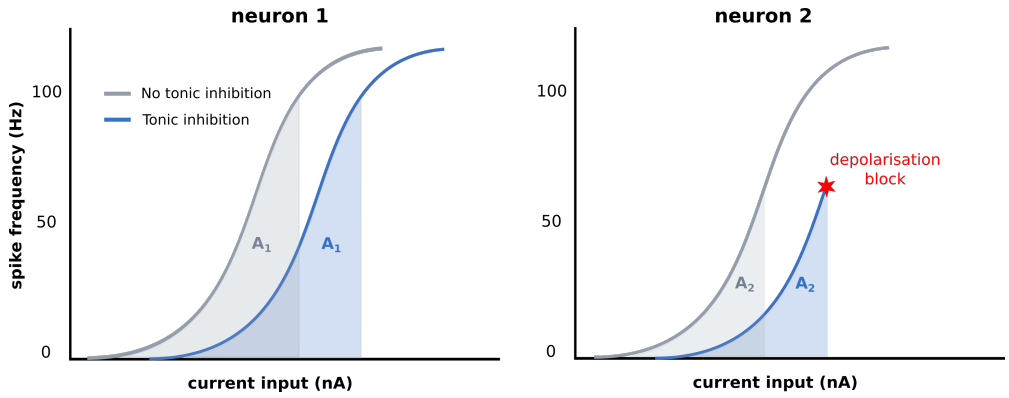

Fig. S10.
I-F curves of two neurons for which tonic inhibition does not change Δ gain (AUC denoted A_1/A_2 for neuron1/neuron2, respectively). In neuron 1, AUC is measured across the same input range with or without tonic inhibition. In neuron 2, AUC is also measured across the same input range, but is restricted by the presence of depolarisation block with tonic inhibition. Although $A_2 < A_1$, there is no change in gain (i.e. Δ gain = 0) in neuron 2. If depolarisation block was ignored, tonic inhibition would generate a dramatic reduction of Δ gain in neuron 2.

SI Methods

1) Detailed neuron modelling

A model of a layer 2/3 Basket Cell (L23BC) available through the Blue Brain Project Neocortical Microcircuit portal was used for single neuron optimisation and simulation[1]. The model contains >200 compartments, a calcium diffusion mechanism and 11 voltage-dependent channel mechanisms based on a Hodgkin-Huxley formulation: fast (transient) sodium and potassium (Na_T & K_T), persistent sodium and potassium (Na_P & K_P), $Kv_{3.1}$, M-current (I_m), hyperpolarisation-activated current (I_h) , calcium-activated potassium (SK), high and low voltage-activated calcium (Ca_H, Ca_L) and a leak current (pas). Parameter values for each mechanism are found in *Markram et al* and references therein[2]. Simulations and analysis were performed using NEURON and Python[3].

Rectifying tonic inhibition was modelled as a voltage-dependent conductance with channel kinetics based on *Pavlov et al*[4]:

$$I_{ton,r} = G_{ton} o\left(v - E_{gaba}\right)$$

$$\frac{\mathrm{d}o}{\mathrm{d}t} = \frac{o - o_\infty(v)}{o_\tau}$$

$$o_\infty(v) = \frac{a(v)}{a(v) + b(v)} \qquad o_\tau(v) = \frac{1}{a(v) + b(b)}$$

$$a(v) = \frac{5(v + 20)}{1 - e^{-0.1(v+20)}} \qquad b(v) = \frac{-1.6(v - 10)}{1 - e^{-0.08(v-10)}}$$

where $I_{ton,r}$ is rectifying tonic current, G_{ton} peak conductance, o activation variable, v membrane voltage, E_{gaba} GABA reversal potential, $o_\infty(v)$ and $o_\tau(v)$ channel activation steady-state and time constant functions, respectively. Tonic inhibition was present in all compartments and G_{ton} retained as a free parameter during model optimisation[5]. E_{gaba} is set to -60mV unless otherwise stated in the manuscript.

G_{ton} upper and lower bounds were based on experimental changes in whole-cell holding current after extra-synaptic $GABA_A$ receptor blockade[6]. This was performed as follows. First, rectifying tonic inhibition was added to a previously optimised L23BC model. E_{GABA} was set to the chloride reversal potential used in the experimental setup. An *in-silico* voltage-clamp was applied at the soma and G_{ton} increased until 'blockade' (setting G_{ton} to 0 S/cm^2) generated similar change in holding current to experimental results. The upper range of experimental results using this approach was 5x10^{-4} S/cm^2. Therefore, G_{ton} was restricted between 0 and 5x10^{-4} S/cm^2 during optimization.

The peak conductance of ion channel mechanisms were optimised using a feature-based multi-objective algorithm implemented through BluePyOpt[7]. Full details of this approach are outlined elsewhere[8,9]. Briefly, models were stimulated with somatic current and values of 32 to 42 electrophysiologic features extracted[10].

For each feature, a Z-score was calculated based on *in-vitro* slice recordings from juvenile rat neocortex. These Z-scores were used as the fitness function for an evolutionary algorithm[8]. Features were optimised to one of three E-types of cortical interneurons: continuous accommodating (cAC), continuous non-accommodating (cNAC) and burst accommodating (bAC)[11,12]. Models were accepted if the sum of fitness scores was under 50. The optimisation algorithm was implemented on a computing cluster based at the Swiss National Supercomputing Centre. 10 models of each E-type (30 models total) were created. For each model, a different random seed was used to implement the optimisation algorithm.

Non-rectifying tonic inhibition was modelled as a passive conductance:

$$I_{ton,nr} = G_{ton,nr}(v - E_{gaba})$$

$I_{ton,nr}$ denotes non-rectifying current and $G_{ton,nr}$ non-rectifying peak conductance. $G_{ton,nr}$ was set to a value that produced an identical change in holding current to G_{ton} after *in-silico* voltage clamp 'block' using an identical approach to above.

2) Gain calculation

I-F relationships of optimised models were obtained using constant current injected at the soma and a point process that generated excitatory conductance noise. Excitatory noise was modelled as an Ornstein-Uhlenbeck stochastic process with parameters based on *Destexhe et al*[13]. I-F curves were derived by increasing mean conductance and variance. To investigate the impact of rectifying tonic inhibition upon neuronal gain, input-frequency curves were calculated for two G_{ton} values: 0 and 0.001 S/cm^2 (referred as 'without' and 'with' tonic inhibition hereon).

Gain was calculated using either the gradient or area under the I-F curve (AUC). Δ gain was defined as the change in gain with tonic inhibition:

$$\Delta \text{ gain } (\%) = 100 \times \frac{Gain_2 - Gain_1}{Gain_1}$$

Where $Gain_1$ denotes I-F gain without tonic inhibition and $Gain_2$ I-F gain with tonic inhibition.

The input range used to calculate AUC was defined from rheobase to a current that elicited either a frequency of 100Hz or produced depolarisation block, and the same input range applied to I-F curves with or without tonic inhibition. This approach ensured that depolarisation block did not produce misleadingly large changes of Δ gain (**SI Appendix Fig. S10**).

The gradient of the I-F curve was calculated after fitting the I-F curve to a Hill-type function [14]:

$$\frac{a(I-b)^c}{d^c+(I-b)^c}$$

where I is input current and a, b, c and d free parameters. Gradient was calculated at a frequency of 20Hz, which represents a spike frequency commonly observed *in-vivo* for interneurons in awake animals [15,16]. In our experimental results gain was also calculated using peak gradient of the I-F curve as an additional measure.

3) Experimental animals

All experimental procedures in this study were conducted in accordance with the Prevention of Cruelty to Animals Act 1986, under the guidelines of the NHMRC Code of Practice for the Care and Use of Animals for Experimental Purposes in Australia and were approved by the Florey Neuroscience Institute Animals Ethics Committee. Homozygous $Sst^{tm2.1(cre)Zjh}$/J mice (Jax Stock number: 013044) or B6;129P2-$Pvalb^{tm1(cre)Arbr}$/J mice (Jax Stock 008069) were crossed with homozygous B6.Cg-Gt(ROSA)26$Sor^{tm14(CAG-tdTomato)Hze}$/J mice (Jax Stock number: 007914) to produce mice that expressed tdTomato specifically in SST or PV expressing interneurons, hereafter termed SST-positive or PV-positive mice.

4) Brain slice preparation

Sst-positive and Pv-positive mice (6-8 weeks old, n = 3 mice) were anesthetized with 2% isoflurane and decapitated. The brain was removed quickly and placed into an iced slurry of cutting solution consisting of (mM): 125 Choline-Cl, 2.5 KCl, 0.4 CaCl2, 6 MgCl2, 1.25 NaH2PO4, 26 NaHCO3, 20 D-glucose saturated with 95% O2 plus 5% CO2. 300 μm coronal cortical slices were cut on a vibratome (VT1200; Leica; Germany) for whole-cell patch-clamp experiments. Slices were incubated at room temperature for a minimum of 1 hour in artificial cerebral spinal fluid (aCSF) consisting of (mM): 125 NaCl, 2.5 KCl, 2 CaCl2, 2 MgCl2, 1.25 NaH2PO4, 26 NaHCO3, 10 D-glucose, saturated with 95% O2 plus 5% CO2 before patching.

5) Whole-cell patch-clamp electrophysiology

Slices cut from Sst-positive and Pv-positive mice were transferred to a submerged recording chamber on an upright microscope (Slicescope Pro 1000; Scientifica, UK) and perfused (2 ml/min) with aCSF at 32 °C. Layer 2/3 interneurons were visually identified using fluorescence targeted patching with infrared-oblique illumination microscopy with a 40x water-immersion objective (Olympus, Japan) and a CCD camera (IEEE 1394; Foculus, Germany). Whole-cell patch-clamp recordings were made in voltage and current clamp modes

using a PatchStar micromanipulator (Scientifica, UK) and an Axon Multiclamp 700B patch-clamp amplifier (MDS, USA). Data were acquired using pClamp software (v10; MDS, USA) with a sampling rate of 50 kHz and low pass Bessel filtered at 10 kHz (Digidata 1440a; Axon). Patch pipettes (4-7 MΩ; GC150F-10; Harvard Instruments, USA) pulled using a Flaming/brown micropipette puller (Model P-1000; Sutter Instruments, USA). For current clamp recordings, patch pipettes were filled with a solution consisting of (mM): 125 K-gluconate, 4 KCl, 2 $MgCl_2$, 10 HEPES, 10 EGTA, and 0.3 GTP-Na (pH 7.3 and 300 mOsm). For voltage clamp recordings, CsCl (15 mM; Sigma, Australia), TEA (10mM; Torcris, Australia) and Qx314 (5 mM; Torcris, Australia) were added to the above internal solution.

6) Pharmacology & characterisation of tonic inhibition

Extracellular blockade of α-amino-3-hydroxy-5-methyl-4-isoxazole-propionic acid (AMPA) and kinate receptors was achieved with 2,3-dihydroxy-6-nitro-7-sulfamoyl-benzo[f]quinoxaline-2,3-dione (NBQX; 50 μM; Sigma, Australia), N-methyl-D-aspartate (NMDA) receptors with (2R)-amino-5-phosphonopentanoate (AP5; 50 μM; Torcris, Australia), γ-aminobutyric acid B ($GABA_B$) receptors with CGP5243 (25 μM; Sigma, Australia), phasic $GABA_A$ receptors with SR95531 (0.5 μM; Sigma, Australia), and extrasynaptic (tonic) $GABA_A$ receptors with picrotoxin (100 μM; Sigma, Australia). GABA (5 μM; Torcris, Australia) was included in the aCSF solution to provide a basal level of GABA agonism.
Once whole-cell configuration was obtained, to characterize firing a holding current was injected to maintain a membrane potential of approximately -70 mV and current steps were applied (-60 to 320 pA steps amplitude in 20 pA increments, 1 s step duration) in current clamp mode. To determine I-V relationships, cells were held at -70 mV and a voltage ramp (from -70 mV to -20 mV, 5 s duration) and voltage step (from -70 mV to 30 mV, 1 s duration) applied. Series resistance and whole-cell capacitance compensation were applied. To be included in the present study a cell had to have an access resistance of less than 20 MΩ and a holding current of less than -200 pA throughout the entire recording. Current and voltage clamp protocols were performed before and after application of picrotoxin. Voltage-dependence of the picrotoxin-sensitive current (ie extra-synaptic $GABA_A$-mediated current) was calculated by subtracting the I-V relationship before and after picrotoxin. Values presented are not corrected for liquid junction potential. The I-V relationship in **SI Appendix Fig. 3d** is normalised for each cell relative to the picrotoxin-sensitive current at -70mV.

7) Experimental data analysis & E-type classification

Experimental data analysis was performed using Axograph X software (Berkeley, USA) and the Electrophys Feature Extraction Library (EFEL) [17]. AP onset was defined when the 1st derivative of the voltage trace exceeds 12V/s for at least 5 consecutive time points. After-hyperpolarization potential (AHP) amplitude was

calculated relative to voltage at AP onset. AP amplitude is calculated relative to minimum AHP voltage and AP height as peak AP voltage. AP half-width (AP-HW) was measured at 50% AP amplitude and AP width at spike threshold. Adaptation index was calculated as the normalised average difference of two consecutive inter-spike intervals (ISIs). Frequency at 100nA is defined as spike frequency at input current 100nA above rheobase. Input resistance was calculated from the voltage deflection relative to baseline that occurred from injection of a -5 pA, 50 ms duration test pulse. Resting membrane potential was defined as the membrane voltage of a cell without injection of a holding current.

Recorded neurons were classified using the Petilla classification by three co-authors of this study with complete inter-observer agreement (AB, CR and SP). Electrophysiologic features of each neuron were extracted at rheobase (with the exception of frequency at 100nA) using the EfEL feature extraction library. Hierarchical clustering was performed using Ward's method with four features: AP-HW, AHP, AI and frequency at 100nA. PV10 was excluded from analysis because it had clearly distinct features to eye compared to other recorded cells, and PV6 excluded because a spike frequency 100nA above rheobase was not obtained with the experimental protocol.

Δ gain was calculated in experimental recordings using the approach in Section 2 after fitting to a Hill function. Due to the sigmoidal shape of the I-F curve in many recorded Sst interneurons, to avoid misleading Δ gain values when calculating AUC the lower input range was defined as the minimum input that elicited a spike frequency above 1Hz.

Phase portraits (**SI Appendix Fig. S4**) were constructed from experimental time-voltage traces at a minimum input that elicited at least 2 AP's. AUC was calculated by interpolating the phase portrait traces and then calculating the enclosed area.

8) Analysis of detailed models

Detailed models were analysed during constant current injection at the soma that elicited a spike frequency of 20Hz with and without dendritic rectifying tonic inhibition. Membrane voltage at adjacent compartments to the soma, and all transmembrane ionic currents at the soma, were recorded. Axial current flow between the soma and a dendrite (d) was calculated from Ohm's law using axial resistivity (R_i), somatic voltage (V_{soma}) and dendritic voltage (V_d). Total axial current at the soma (I_{Ax}) is the sum of all axial currents:

$$I_{Ax} = \sum^{d} \frac{V_{soma} - V_d}{R_i}$$

I_{Ax} was adjusted for somatic surface area and expressed as current density (**Fig. 5**). Total membrane current is defined as the sum of ionic (I_{Ion}), axial and injected current (I_{stim}). When considering the current-balance

equation, total membrane current is equivalent to the first derivative of the time-voltage trace adjusted for somatic membrane capacitance (c):

$$c\dot{v} = I_{Ion} + I_{Ax} + I_{stim}$$

The ISI was defined as the interval between the onset of two consecutive AP's (Section 6) during steady-state firing after a 1 second current injection. Δ total membrane current was calculated by subtracting total membrane current with and without tonic inhibition during an ISI (**Fig. 5b**). To ensure calculation of Δ total membrane current was not subject to numerical error, simulations were performed with a fixed time-step of shorter duration until differences in waveform were no longer visible by eye. Results presented use a time step of 0.001ms. Changes in axial (Δ axial) and individual transmembrane ionic currents during an ISI were calculated using the same approach (**Fig. 5e**).

To determine the contribution of axial and transmembrane ionic currents to Δ total membrane current over T_1 & T_2, the normalised change in membrane charge transfer (Δ charge) was calculated. This represents the relative difference in charge deposited across the membrane for a given ionic species in the presence of tonic inhibition. For example, the contribution of axial charge transfer (Δ axial charge) over period T_1 is given by:

$$\Delta \text{ axial charge} = \frac{\int^{T_1} \Delta \text{ axial current}}{\int^{T_1} |\Delta \text{ Na current}| + \int^{T_1} |\Delta \text{ K current}| + \int^{T_1} |\Delta \text{ axial current}|}$$

Where calcium current is omitted as its contribution is negligible. The contribution of all ionic currents over period T_1 and T_2 was calculated in the same manner.

The conductance densities of voltage-dependent potassium channels in **SI Appendix Fig. S5e&f** were obtained by calculating mean conductance densities across the soma & axon in all models. Dendritic conductance's were excluded from this analysis for the following reasons: 1) conductance densities in dendrites were at least an order of magnitude lower (except I_m which was ~4-fold lower), and 2) our analysis shows that axial current reduces activation of potassium conductance's at the soma to modulate AP activity. The dendrite in **SI Appendix Fig. S9** was modelled in NEURON using a single cable 400µm long while varying the spatial extent of tonic inhibition throughout the membrane. An AP was simulated by injecting a 2ms current that elicited a membrane potential of 20mV using an SEClamp point process. Axial current and charge were calculated using the same approach above.

9) Simplified neuron modelling

Simplified neuron models were developed in three stages. First, channel mechanism used in detailed models were re-expressed in terms of a variable that evolves over one of three time scales: fast (v), slow (w) and ultraslow (u). Second, single compartment models containing these mechanisms were optimised to fit the features of a detailed bAC and cNAC model with and without tonic inhibition. Finally, optimised simple models were only analysed if the model 'with' tonic inhibition exhibited enhanced AP repolarisation and early recovery from AP repolarisation compared to the model 'without' tonic inhibition, similar to their detailed counterparts.

Channel mechanisms were simplified using a technique based on separation of timescales and equivalent voltages[18,19]. First, Na_T channel activation responsible for AP upstroke is considered instantaneous with respect to voltage (v). Using a standard Hodgkin-Huxley formulation, the Na_T activation variable (m) is therefore set to its steady-state value ($m_{NaT,\infty}(v)$) and Na_T current density (I_{NaT}) given by:

$$I_{NaT} = G_{NaT} m_{NaT,\infty}(v)^3 h(v - E_{Na})$$

where G_{NaT} is peak Na_T channel conductance, $m_{NaT,\infty}(v)$ steady-state Na_T conductance, E_{Na} Na reversal potential and h_{NaT} the Na_T channel inactivation variable.

Next, the K_P activation variable (w) was used in the bAC model to govern dynamics of other variables evolving over a slow time-scale that generate the AP downstroke, AHP and ISI: Na_T inactivation, $Kv_{3.1}$ activation, Na_P activation and I_h channel activation. For the cNAC model, AP feature could only be reproduced if w was governed by kinetics of $Kv_{3.1}$ activation. For the bAC model, the inverse of the K_P steady-state function ($w_\infty(v)$) describes an equivalent voltage (v_w) for a given value of w. I_{Kp} and I_{Na}, the latter re-expressed in terms of v_w, is therefore given by:

$$I_{NaT} = G_{NaT} m_{NaT,\infty}(v)^3 h(v - E_{Na})$$

$$I_{NaT} = G_{NaT} m_{NaT,\infty}(v)^3 h_{NaT,\infty}(v_w)(v - E_{Na})$$

$$I_{K_P} = G_{K_P} w(v - E_K)$$

$$\frac{\mathrm{d}w}{\mathrm{d}t} = \frac{w - w_\infty(v)}{w_\tau(v)} \qquad v_w = w_\infty^{-1}(w)$$

where $w_\tau(v)$ is the K_P time constant function and $h_{NaT,\infty}(v_w)$ the Na_T inactivation variable steady-state function. An identical formulation was used for the simple cNAC model, with v_w instead given by the inverse of the $Kv_{3.1}$ steady-state variable.

Finally, I_m channel activation (u) evolves over an ultraslow time scale and generates features of spike-frequency adaptation.

The current-balance equation for the full, simplified bAC model is given by:

$$c\dot{v} = G_{NaT}m_{NaT,\infty}(v)^3 h_{NaT,\infty}(v_w)(v - E_{Na}) + G_{K_P}w(v - E_K) + G_{K_V}m_{K_V,\infty}(v_w)(v - E_K) + G_{N_P}m_{N_P,\infty}(v - E_{Na}) + G_{I_h}m_{I_h,\infty}(v_w)\left(v - E_{I_h}\right) + G_{I_m}u\left(v - E_{I_m}\right) + G_{pas}\left(v - E_{pas}\right) + I_{stim}$$

$$\frac{\mathrm{d}w}{\mathrm{d}t} = \frac{w - w_\infty(v)}{w_\tau(v)} \qquad \frac{\mathrm{d}u}{\mathrm{d}t} = \frac{u - u_\infty(v)}{u_\tau(v)} \qquad v_w = w_\infty^{-1}(w)$$

where c is membrane capacitance, I_{stim} input current and subscripts N_P, K_V and *pas* refer to persistent Na, $K_{V3.1}$ and leak current respectively.

Parameters of simple models were optimised using a similar approach to Section 1. First, features used to optimise detailed models were extracted from a detailed bAC and cNAC model with and without tonic inhibition using EFEL. These features were used as means for the multi-objective function. The standard deviation for each feature was identical to those used during fitting for detailed models. For each optimised simple model, the sum of all feature errors was under 20. Ie the simplified models replicated the features of detailed models more accurately than the detailed models replicated features from *in-vitro* recordings.

Phase plane analysis of the *v*-*w* subsystem of simple models was performed after freezing the ultraslow variable (*u*). This approached is justified mathematically since the time constants of each variable are separated by at least an order of magnitude[19]. Phase plane analysis was performed using XPPAUT[20]. In **Fig. 6e** (& SI Appendix **Fig. 5e**) the bottleneck is defined as a period of the trajectory that accounts for 90% of the duration of the orbit at rheobase.

10) Network modelling

A rate-based model developed by *Hayut et al* consisting of a population of excitatory pyramidal cells (PC) and SST interneurons was used for network simulations[21]. PC and SST populations receive reciprocal synaptic connections and the PC population recurrent excitatory connections and a constant input I_{stim}. Short-term synaptic plasticity uses a *Tsodyks-Markram* formulation with 3 dynamic variables: fraction of open channels (s), fraction of vesicles available for release (x) and a utilisation parameter (u)[22]. Other synaptic parameters include conductance (g), initial probability of vesicle release (U), decay time constant of the post-synaptic current (τ_s) and recovery time constants from facilitation and depression (τ_f, τ_r respectively). Synaptic dynamics from neuronal population j to i are as follows:

$$\frac{ds_{ij}}{dt} = -\frac{s_{ij}}{\tau_{s,ij}} + u_{ij}x_{ij}M_j$$

$$\frac{dx_{ij}}{dt} = -\frac{1 - x_{ij}}{\tau_{r,ij}} - u_{ij}x_{ij}M_j$$

$$\frac{du_{ij}}{dt} = -\frac{U_{ij} - u_{ij}}{\tau_{f,ij}} + U_{ij}(1 - u_{ij})M_j$$

Mean firing rates (M) for PC and SST neuronal populations, denoted by subscripts P and S, are given by:

$$M_P = \beta_P[I_{stim} + g_{PP}s_{PP} - g_{PS}s_{PS} - \theta_P]_+$$

$$M_S = \beta_S[g_{SP} - \theta_S]_+$$

Where θ determines neuronal rheobase, β neuronal gain and $[]_+$ is the linear-threshold function:

$$[f(x)]_+ = \begin{cases} f(x) \text{ for } f(x) > 0 \\ 0 \text{ for } f(x) < 0 \end{cases}$$

Synapses from PC to SST neurons are facilitating, and those from SST to PC neurons depressing. All parameters used are identical to those in *Hayut et al* unless otherwise stated[21].

The sensitivity analysis in **SI Appendix Fig. S7** was performed by simulating network activity across different g_{pp} and I_{stim} values before and after a 20% and 40% increase in β_s. Network simulations were performed using PyDSTool[23]. The network was considered to exhibit sustained gamma-frequency oscillations if oscillations persisted for over 1000 ms. Oscillations lasting between 500-1000ms were considered transient.

11) Statistics

Results are presented as mean ± s.e.m. We based sample sizes for our modelling results on a pilot study of one fast spiking and one non-fast spiking model. Here, a Δ gain of ~ -10% and +10% was observed. Assuming variance of 5% we calculated a sample of at least 8 to ensure adequate power. For experimental studies, we used a similar sample size to our models under the assumption our models were predictive. Our sample sizes are also comparable to those reported in previous studies exploring the impact of a neuromodulator upon single neuron excitability [24–26]. Data was assessed for normality using the Shapiro-Wilk test. Significant changes of Δ gain for individual E-types, changes of AP features and phase plot AUC were calculated using either 1-sample *t*-test or Wilcoxon signed-rank test. Comparison between fast spiking and non-fast spiking E-types and conductance density ratio's used Welch's *t*-test or Mann-Whitney U test. Differences were considered significant if $*P < 0.05$, $**P < 0.01$, $***P < 0.001$. n.s. denotes not significant.

Tables

Table S1.

Cell	E-type	HW (ms)	AHP (mV)	AI	Freq (Hz)	ISI CV	Δ gain (AUC)	Δ gain (20Hz)	Δ gain (peak)
Sst1	cAC	0.81	12.37	0.035	76	0.12	48.4	127.7	123.6
Sst2	cAC	0.907	8.55	0.058	76	0.24	26.4	44.8	45.5
Sst3	cAC	0.597	10.4	0.166	66	0.16	12.9	18.3	15.9
Sst4	cAC	0.72	12.9	0.073	52	0.26	10.8	19.4	20.3
Sst5	cAC	0.72	7.86	0.07	74	0.2	9.9	12.3	21.1
Sst6	cAC	0.48	9.05	0.083	54	0.32	13.0	11.4	8.7
Sst7	cAC	0.89	14.57	0.058	60	0.16	4.8	-3.6	5.5
Sst8	cAC	0.54	17.37	0.047	77	0.37	4.5	16.8	1.9
Sst9	naNFS	0.76	16.75	0.0045	86	0.08	12.5	4.3	9.5
Sst10	naNFS	1.16	17.42	-0.03	50	0.13	7.1	3.0	3.0
Sst11	naNFS	0.47	19.19	0.006	55	0.18	4.9	13.1	13.4
Pv1	cNAC	0.37	22.1	0.0037	140	0.12	-13.2	-14.1	-18.1
Pv2	cNAC	0.406	21.38	0.0016	150	0.09	-11.4	-24.7	-27.2
Pv3	dNAC	0.37	22.15	0.011	110	0.13	-18.8	-27.4	-18.0
Pv4	dNAC	0.35	18.8	-0.0008	160	0.11	-37.9	-73.8	-96.4
Pv5	dNAC	0.42	25.9	0.014	92	0.08	-2.3	-7.1	0.7
Pv6	dNAC	0.347	24.21	0.001	-	0.23	-27.1	-34.5	-50.6
Pv7	dNAC	0.36	22.46	0.011	88	0.16	1.2	0.1	2.3
Pv8	dNAC	0.37	22.34	0.019	108	0.34	-7.9	-21.8	-18.0
Pv9	cAC	0.61	14.47	0.026	80	0.22	10.6	16.0	12.9
Pv10	bIR	0.296	19.59	0.0056	110	0.56	25.7	39.3	29.8

Electrophysiologic characteristics of recorded interneurons used for E-type classification and changes of gain with tonic inhibition. **Abbreviations**. E-type = Petilla electrophysiologic subtype; HW = AP half-width; AHP = afterhyperpolarisation depth; AI = adaptation index; Freq = spike frequency at 100nA above rheobase; ISI CV = inter-spike interval coefficient of variation; Δ gain = change in gain with tonic inhibition calculated using area under curve (AUC), gradient at 20Hz (20Hz) or peak gradient (peak).

Table S2.

Parameter	bAC (none)	bAC (tonic)	cNAC (none)	cNAC (tonic)
c	0.0027	0.0027	0.003	0.003
G_{NaT}	1.005	1.005	2.98	2.88
G_{Kp}	1.072	1.072	0.054	0.054
G_{Kv}	0.0778	0.0778	0.366	0.366
G_{Np}	$3e^{-5}$	$3e^{-5}$	$1.1e^{-6}$	$1.1e^{-6}$
G_{Ih}	0.02525	0.0179	0.0023	0.004
G_{Im}	0.0542	0.0356	0.00032	0.00032
G_{pas}	$3.9e^{-5}$	$3.9e^{-5}$	$2.4e^{-5}$	$6.5e^{-5}$
E_{NaT}	2.57	2.57	5.74	5.74
E_{Kp}	-75.2	-75.2	-67.7	-72.1
E_{Kv}	-74.5	-74.5	-75.5	-75.5
E_{Np}	5.6	5.6	7.9	7.9
E_{Ih}	-83.9	-79.8	-86.5	-85.9
E_{Im}	-81.0	-81.0	-55.2	-55.2
E_{pas}	-88.0	-88.0	-40.4	-77.7
V_{1NaTm}	-46.96	-45.8	-32.5	-32.5
V_{2NaTm}	6.0	6.0	7.17	7.2
V_{1NaTh}	-62.5	-62.7	-56.6	-57.6
V_{2NaTh}	6.0	6.0	7.1	7.0
V_{1Kp}	-1.0	-1.0	2.3	2.3
V_{2Kp}	12.0	12.0	12.9	12.9
V_{1Np}	-52.6	-52.6	-52.6	-52.6
V_{2Np}	-4.6	-4.6	-4.6	-4.6
V_{1Kv}	18.7	18.7	31.4	31.4
V_{2Kv}	9.7	9.7	10.4	10.4
V_{1Ih}	-109.7	-109.7	-109.7	-109.7
V_{2Ih}	10.06	10.06	10.06	10.06
V_{1Im}	31.27	31.27	35.0	35.0
V_{2Im}	3.13	3.13	10.0	10.0
u_τ	2205	3191	562	562

Parameter values for single compartment models optimised to replicate features of detailed bAC & cNAC models with (`tonic') and without (`none') rectifying tonic inhibition. **Abbreviations**. c = capacitance (F/cm^2); G_X = peak conductance (S/cm^2); E_X = reversal potential (mV); V_1/V_2 = half voltage / slope of activation function, respectively; $u_\tau = I_m$ time constant.

SI references

1. Ramaswamy, S. *et al.* The neocortical microcircuit collaboration portal: a resource for rat somatosensory cortex. *Front. Neural Circuits* **9**, (2015).
2. Markram, H. *et al.* Reconstruction and Simulation of Neocortical Microcircuitry. *Cell* **163**, 456–92 (2015).
3. Hines, M. L. & Carnevale, N. T. The NEURON simulation environment. *Neural Comput.* **9**, 1179–1209 (1997).
4. Pavlov, I., Savtchenko, L. P., Kullmann, D. M., Semyanov, A. & Walker, M. C. Outwardly rectifying tonically active GABA(A) receptors in pyramidal cells modulate neuronal offset, not gain. *J. Neurosci.* **29**, 15341–15350 (2009).
5. Kasugai, Y. *et al.* Quantitative localisation of synaptic and extrasynaptic GABA(A) receptor subunits on hippocampal pyramidal cells by freeze-fracture replica immunolabelling. *Eur. J. Neurosci.* **32**, 1868–1888 (2010).
6. Lee, V. & Maguire, J. The impact of tonic GABA(A) receptor-mediated inhibition on neuronal excitability varies across brain region and cell type. *Front Neural Circuits* **8**, 3 (2014).
7. Rössert, C. *et al.* BluePyOpt : Leveraging Open Source Software and Cloud Infrastructure to Optimise Model Parameters in Neuroscience. *Front. Neuroinform.* **10**, (2016).
8. Druckmann, S., Banitt, Y., Gidon, A., Sch, F. & Markram, H. A novel multiple objective optimization framework for constraining conductance-based neuron models. *Front. Neurosci.* **1**, (2007).
9. Hay, E., Hill, S., Schürmann, F., Markram, H. & Segev, I. Models of neocortical layer 5b pyramidal cells capturing a wide range of dendritic and perisomatic active properties. *PLoS Comput. Biol.* **7**, e1002107 (2011).
10. Druckmann, S. *et al.* Effective Stimuli for Constructing Reliable Neuron Models. *PLOS Comput. Biol.* **7**, 534–542 (2011).
11. Ascoli, G. a *et al.* Petilla terminology: nomenclature of features of GABAergic interneurons of the cerebral cortex. *Nat. Rev. Neurosci.* **9**, 557–568 (2008).
12. Markram, H., Toledo-rodriguez, M., Wang, Y. & Gupta, A. Interneurons of the neocortical inhibitory system. *Nat. Rev. Neurosci.* **5**, 793–807 (2004).
13. Destexhe, A., Rudolph, M., Fellous, J. M. & Sejnowski, T. J. Fluctuating synaptic conductances recreate in vivo-like activity in neocortical neurons. *Neuroscience* **107**, 13–24 (2001).
14. Silver, R. A. Neuronal arithmetic. *Nat. Rev. Neurosci.* **11**, 474–489 (2010).
15. Kvitsiani, D. *et al.* Distinct behavioural and network correlates of two interneuron types in prefrontal cortex. *Nature* **498**, 363–366 (2013).
16. Fanselow, E. E. & Connors, B. W. The Roles of Somatostatin-Expressing (GIN) and Fast-Spiking Inhibitory Interneurons in UP-DOWN States of Mouse Neocortex. *J. Neurophysiol.* **104**, 596–606 (2010).
17. Electrophys Feature Extraction Library. Available at: https://github.com/BlueBrain/eFEL.
18. Drion, G., O'Leary, T. & Marder, E. Ion channel degeneracy enables robust and tunable neuronal firing rates. *Proc. Natl. Acad. Sci.* **112**, E5361–E5370 (2015).
19. Franci, A., Drion, G. & Sepulchre, R. Modeling the modulation of neuronal bursting: a singularity theory approach. *SIAM J Appl Dyn Syst* **13**, 798–829 (2013).
20. Ermentrout, B. & Mahajan, A. Simulating, Analyzing, and Animating Dynamical Systems: A Guide to XPPAUT for Researchers and Students. *Appl. Mech. Rev.* **56**, B53 (2003).
21. Hayut, I., Fanselow, E. E., Connors, B. W. & Golomb, D. LTS and FS inhibitory interneurons, short-term synaptic plasticity, and cortical circuit dynamics. *PLoS Comput. Biol.* **7**, e1002248 (2011).
22. Tsodyks, M. & Markram, H. Neural Networks with Dynamic Synapses. *Neural Comput.* **835**, 821–835 (1998).
23. Clewly, R., Sherwood, W., LaMar, M. & Guckenheimer, J. PyDSTool, a software environment for dynamical systems modeling. (2007). Available at: http://pydstool.sourceforge.net.
24. Xiang, Z., Huguenard, J. R. & Prince, D. A. Cholinergic switching within neocortical inhibitory networks. *Science (80-.).* **281**, 985–988 (1998).
25. Song, I., Savtchenko, L. & Semyanov, A. Tonic excitation or inhibition is set by GABA(A)

conductance in hippocampal interneurons. *Nat. Commun.* **2**, 376 (2011).
26. Sanchez, G., Rodriguez, M. J., Pomata, P., Rela, L. & Murer, M. G. Reduction of an Afterhyperpolarization Current Increases Excitability in Striatal Cholinergic Interneurons in Rat Parkinsonism. *J. Neurosci.* **31**, 6553–6564 (2011).